Extrusion dynamics of deep-water volcanoes revealed by 3D seismic data

Qiliang Sun[1,2,3], Christopher A-L. Jackson[4], Craig Magee[4,5], Samuel J. Mitchell[6] and Xinong Xie[1,3]

[1]Key Laboratory of Tectonics and Petroleum Resources, China University of Geosciences (Wuhan), Ministry of Education, Wuhan 430074, China;

[2]Laboratory for Marine Mineral Resources, Qingdao National Laboratory for Marine Science and Technology, Qingdao 266061, China;

[3]College of Marine Science and Technology, China University of Geosciences (Wuhan), Wuhan, Hubei 430074, PR China;

[4]Basins Research Group (BRG), Department of Earth Science &Engineering, Imperial College, London, SW7 2BP, UK

[5]School of Earth and Environment, University of Leeds, Leeds, LS2 9JT, UK

[6]School of Earth Sciences, University of Bristol, Bristol, BS8 1RJ UK

Abstract

Submarine volcanism accounts for c. 75% of the Earth's volcanic activity. Yet difficulties with imaging their exteriors and interiors mean the extrusion dynamics and erupted volumes of deep-water volcanoes remain poorly understood. Here, we use high-resolution 3-D seismic reflection data to examine the external and internal geometry, and extrusion dynamics of two Late Miocene-Quaternary, deep-water (>2 km emplacement depth) volcanoes buried beneath 55–330 m of sedimentary strata in the South China Sea. The volcanoes have crater-like bases, which truncate

23 underlying strata and suggest extrusion was initially explosive, and erupted lava flows that feed

24 lobate lava fans. The lava flows are >9 km long and contain lava tubes that have rugged basal

25 contacts defined by ~90±23 m high erosional ramps. We suggest the lava flows eroded down into

26 and were emplaced within wet, unconsolidated, near-seafloor sediments. Extrusion dynamics were

27 likely controlled by low magma viscosities as a result of increased dissolved H_2O due to high

28 hydrostatic pressure, and soft, near-seabed sediments, which collectively are characteristic of deep-

29 water environments. We calculate that long run-out lava flows account for 50–97% of the total

30 erupted volume, with a surprisingly minor component (~3–50%) being preserved in the main

31 volcanic edifice. Accurate estimates of erupted volumes therefore require knowledge of volcano

32 and lava basal surface morphology. We conclude that 3D seismic reflection data is a powerful tool

33 for constraining the geometry, volumes, and extrusion dynamics of ancient or active deep-water

34 volcanoes and lava flows.

36 **Keywords**

37 Volcano, deep-water, lava flow, seismic reflection, South China Sea

39 # 1. Introduction

40 The external morphology of volcanoes and their eruptive products reflect, and provide insights

41 into, the processes controlling magma extrusion and volcano construction (e.g. Walker, 1993;

42 Planke et al., 2000; Grosse and Kervyn, 2018). By collecting high-resolution, quantitative data on

43 the morphology of modern volcanic edifices and surrounding lava flows from airborne/shuttle radar

44 topography or time-lapse multi-beam bathymetry, we can estimate erupted volumes, at least for

45 individual eruptive episodes (e.g. Holcomb et al., 1988; Walker, 1993; Goto and McPhie, 2004;

46 Cocchi et al., 2016; Somoza et al., 2017; Allen et al., 2018; Chadwick et al., 2018; Grosse and

47 Kervyn, 2018). Whilst remote sensing data capture the external morphology of volcanoes and lava

48 flows, both before, during, and after eruptions, they do not image their basal surface or internal

49 architecture. Without access to the full 3D structure of these extrusive systems, it is difficult to assess

50 the accuracy of estimated volumes of total erupted materials over multiple eruptive episodes, and to

51 thus test long-term volcano growth and lava emplacement models.

52   Several studies demonstrate that seismic reflection data can be used to map the external

53 morphology and internal architecture of buried volcanoes in 3D (e.g. Planke et al., 2000; Calvès et

54 al., 2011; Jackson, 2012; Magee et al., 2013; Arnulf et al., 2014; Reynolds et al., 2017; Arnulf et al.,

55 2018). To-date, most seismic-based studies have focused on volcanoes formed in sub-aerial or

56 shallow-marine environments (e.g. Planke et al., 2000; Jackson, 2012; Magee et al., 2013; Keen et

57 al., 2014; Reynolds et al., 2018), although seismic reflection surveys have been used to image the

58 shallowly buried flanks of deep-water volcanoes (e.g. Funck et al. 1996). The 3D geometry, internal

59 structure, and volume of deep-water volcanoes thus remain poorly documented. Without such

60 information on the structure of deep-water volcanoes, we cannot assess how they grow or what

61 hazard they may pose (e.g. tsunamis induced by flank collapse, seabed deformation and instability

62 induced by highly explosive eruptions).

63   We use high-resolution 3D seismic reflection data to examine the external morphology and

64 internal architecture of two, Late Miocene-Quaternary submarine volcanoes that were emplaced in

65 deep-water (>2.0 km) on highly stretched continental crust in the northern South China Sea (Fig. 1).

66 The volcanoes and associated lava flows are now buried by a ~55–330 m thick sedimentary

succession (Fig. 1). These two volcanoes are physically isolated and appear to have been fed by

independent, sub-volcanic intrusive bodies (i.e. sills; see below); we can thus confidently

characterize each individual volcano and its associated lava flows (Fig. 1b). By interpreting volcano

and lava flow 3D structure, distribution, and size, we aim to determine extrusion dynamics, calculate

accurate erupted volumes, and relate our findings to modern deep-water volcanoes studied using

bathymetry and remote sensing data. We show that the basal surfaces of these volcanic edifices and

lava flows are erosive, with 50–97% of the total erupted material hosted within the latter; i.e. the

volcano edifices only comprise a small portion of the total erupted volume. We suggest the high

hydrostatic pressure of the deep-water environment controlled melt H_2O content and internal lava

viscosity, effusion rate and, consequently, volcano and lava flow morphology and run-out distance.

Our results also show that erupted volumes calculated from airborne/shuttle radar topography or

time-lapse multi-beam bathymetry data, without knowledge of detailed geometry of the basal

surfaces of the lava flows and the volcanoes themselves, may be grossly underestimated, particularly

if extrusion was explosive and/or involved erosion of the seabed.

2. Geological setting

The study area is located south of Pearl River Mouth Basin, on the northern, highly stretched

continental crust of the South China Sea (Franke, 2013; Zhao et al., 2016) (Fig. 1a). The South

China Sea was an area of subduction in the late Mesozoic, before the onset of continental rifting

and subsequent seafloor spreading (~33-15 Myr) in the Cenozoic (e.g. Taylor and Hayes, 1983;

Briais et al., 1993; Franke et al., 2014; Li et al., 2014; Sun et al., 2014a; Ding and Li, 2016). A lack

of seaward-dipping reflections (SDRs) and low volumes of rift-related igneous rocks, suggest the

89   northern part of the South China Sea is a magma-poor margin (e.g. Clift et al., 2001; Yan et al.,

90   2006; Cameselle et al., 2017). Seafloor spreading ceased at ~15 Ma (Li et al., 2014), with post-rift

91   thermal cooling driving subsidence of the northern South China Sea margin since the Early Miocene

92   (Ru and Pigott, 1986; Yu, 1994). During this phase of thermal subsidence, the Dongsha Event (~5.3

93   Ma) occurred, which involved widespread uplift and normal faulting (e.g. Lüdmann et al., 2001).

94   Several mechanisms may have triggered the Dongsha Event, including the collision between Taiwan

95   and the East Asian continent (Lüdmann et al., 2001; Hall, 2002), isostatic rebound (Zhao et al.,

96   2012), post-rift magmatism (Franke, 2013), lithospheric bending (Wu et al., 2014), and/or

97   subduction of the South China Sea beneath the Philippine Sea plate (Xie et al., 2017).

98   Post-spreading magmatism in the South China Sea may reflect ascent of magma triggered by

99   subduction of the South China Sea along the Manila trench and collision with Taiwan Island

100   (Lüdmann et al., 2001), convective removal of continental lithosphere by warm asthenosphere

101   (Lester et al., 2014), or magma ascent from a high-velocity layer in the lower crust fed by the Hainan

102   mantle plume (Xia et al., 2016; Fan et al., 2017). Volcanoes generated by post-rift magmatism in

103   the early Miocene and Quaternary were emplaced both onshore and offshore (e.g. Zou et al., 1995;

104   Yan et al., 2006; Franke, 2013; Li et al., 2014; Sun et al., 2014b; Zhao et al., 2014, 2016; Fan et al.,

105   2017), with the latter typically extruded onto the continental slope in relatively shallow water depths

106   (<300 m; Yan et al., 2006; Zhao et al., 2016). Boreholes reveal these shallow-water volcanoes are

107   composed of basalt, dacite, and rhyolitic tuff (Li and Liang, 1994; Yan et al., 2006; Zhao et al.,

108   2016). In addition to the onshore and shallow-water volcanoes, several volcanoes were emplaced

109   further basinwards on the continental slope in deeper water, close to the Continent-Ocean Boundary

110   (COB; Fig. 1) (Clift et al., 2001; Wang et al., 2006; Cameselle et al., 2017). We examine two of

these deep-water volcanoes, which are situated in an area currently characterized by water depths of 1850–2680 m and are now buried beneath sedimentary strata up to 330 m thick (Fig. 1). Micropalaeontological data from the Pearl River Mouth Basin (Xu et al., 1995; Qin, 1996), and microfauna data from ODP borehole sites 1146 and 1148, indicate the Middle Miocene (16.5 Ma) to Recent, nanofossil-bearing clays overlying the volcanoes were deposited in a deep-water setting (1.0–3.0 km; Wang et al., 2000).

3. Data and Methods

We use a time-migrated 3D seismic reflection survey acquired in 2012 and covering an area of ~350 km^2 (Fig. 1b). The seismic data are zero-phase processed and displayed with SEG (Society of Exploration Geophysicists) normal polarity, whereby a downward increase in acoustic impedance (a function of rock velocity and density) corresponds to a positive reflection event (red on seismic profiles) (e.g. Brown, 2004). The inline and crossline spacing are 25 m, respectively. The seismic data have a dominant frequency in the interval of interest (i.e. 0–400 ms two-way time (twt)) of ~40 Hz.

Stacking velocities are not available for the survey and no wells intersect the studied Late Miocene-Quaternary buried deep-water volcanic features. We thus have no direct observations of the composition or velocities of the seismically imaged volcanic materials. Depth-conversion of volcano edifice and lava flow thickness measurements in milliseconds (twt) to meters is therefore based on velocity estimates, which introduces some uncertainty into our erupted volume calculations. To derive a reasonable velocity estimate, we use velocity data obtained from boreholes (i.e. BY7-1 and U1431) (Li et al., 2015; Zhao et al., 2016) and OBS (Ocean Bottom Seismometer)

133 profiles (Yan et al., 2001; Wang et al., 2006; Chiu, 2010; Wei et al., 2011) in the South China Sea.

134 The boreholes, which are situated >300 km away from our study area, intersect buried basaltic

135 volcanoes with p-wave velocities of ~4.5 km/s (BY7-1; Zhao et al., 2016) and ~3.0–5.0 km/s (IODP

136 U1431; Li et al., 2015). OBS profiles reveal that submarine volcanoes located 140 km from the

137 study area (Fig. 1a) typically have p-wave velocities of >3.0 km/s, and occasionally up to ~5.5 km/s

138 (Yan et al., 2001; Wang et al., 2006; Chiu, 2010; Wei et al., 2011). These p-wave velocities of ~3.0–

139 5.5 km/s are consistent with p-wave velocity data for shallow-water, mafic volcanoes located

140 offshore western India (~3.3–5.5 km/s; Calvès et al., 2011), and southern Australia in the Bight

141 (~2.4–6.7 km/s, with an average velocity of 4.0 km/s; Magee et al. 2013) and Bass (~2.2–4.0 km/s

142 with an average of 3.0 km/s; Reynolds et al. 2018) basins. Based on these velocity data, we assume

143 the imaged volcanic deposits here have mafic compositions and p-wave velocities of 4.0 (±1.0) km/s.

144 It is important to note that using a range of estimated velocities does not affect our calculation of

145 the *relative* amount of material contained within volcanic edifices versus the flanking lava flows.

146   We calculate a vertical resolution ($\lambda/4$) of ~10 m for the sedimentary strata overlying the volcanic

147 materials, given a dominant frequency of 40 Hz and assuming a seismic velocity of 2.2 km/s for the

148 nanofossil-bearing clay (based on seismic refraction profiles OBS1993, Yan et al., 2001; OBS2001,

149 Wang et al., 2006; OBS2006-3, Wei et al., 2011). The calculated vertical resolution for the volcanic

150 materials is 19–31 m, based on a dominant frequency of 40 Hz and estimated seismic velocities of

151 4.0 (±1.0) km/s. The top and base of volcanic structures can be distinguished in seismic reflection

152 data when their thickness is greater than the estimated vertical resolution (i.e. 19–31 m) (Brown,

153 2004). Volcanic structures with thicknesses below the vertical resolution, but above the detection

154 limit (i.e. $\lambda/8 = 10–16$ m), are imaged as tuned reflection packages whereby reflections from their

top and base contacts interfere on their return to the surface and cannot be distinguished (Brown,

2004). The lava flows we image are typically >2 seismic reflection thick (>41±10 m), suggesting

they too are thicker than the tuning thickness and are represented by discrete top and basal

reflections (Tables 1-3).

We used a regional 2D seismic profile and interpreted four seismic surfaces tied to ODP Site 1146,

which is located ~65 km west of the study area (Figs. 1a, 2), and two horizons locally mappable

around the volcanoes: T0 (~2.58 Ma), T1 (~5.3 Ma), TRa (~6.5 Ma), and TRb (~8.2 Ma), TM (top

of the volcanic material) and BM (base of the volcanic material). The youngest age of the volcanoes

and associated lava flows are determined using the first seismic reflection that onlaps or overlies

them (Fig. 3). After mapping TM and BM, we calculated the volumes of the volcanic features

(Tables 1-4), with errors largely arising from uncertainties in the velocities (4.0±1.0 km/s) used to

undertake the depth conversion (see above).

Root mean square (RMS) amplitude extractions and slices through a variance volume were used

to constrain the geometry, scale, and distribution of the submarine volcanoes (Figs. 3-8). The RMS

amplitude attribute computes the square root of the sum of squared amplitudes, divided by the

number of samples within the specified window used; put simply, the RMS attribute measures the

reflectivity of a given thickness of seismic data (Fig. 4a) (Brown, 2004). The variance attribute is

free of interpreter bias because it is directly derived from the processed data (Fig. 5). Variance

measures the variability in shape between seismic traces; this can be done in a specified window

along a picked horizon or within a full 3D seismic volume. Variance is typically used to map

structural and stratigraphic discontinuities related to, for example, faults and channels (Brown,

2004).

177

4. Seismic expression and interpretation of igneous features

179

4.1. Observations

181   We identify three main types of seismic structures and associated facies related to these buried

deep-water volcanoes: (1) Seismic Facies 1 (SF1): two (V1 and V2) conical-shaped features up to

~202 ms twt (~404±101 m) thick, which internally are weakly-to-moderately reflective or chaotic

with distinguished reflections downlapping onto BM, capped by a positive polarity, high-amplitude

reflection (TM) onlapped by overlying strata (Figs. 3a, 7); (2) Seismic Facies 2 (SF2): ribbon-like,

broadly strata-concordant, high-amplitude, positive polarity reflections, which emanate from the

conical structures (SF1) and extend up to ~9.2 km downslope (Figs. 3a-b, 6-7); and (3) Seismic

Facies 3 (SF3): saucer-shaped, strata-discordant, high-amplitude reflections situated beneath SF1

and SF2 (Fig. 6).

190

4.2. Interpretations

192   The conical shape of SF1 and downlap of its internal reflections (where developed) onto BM,

coupled with onlap of overlying reflections onto TM, suggest SF1 is an extrusive rather than

intrusive feature. SF1 is similar in terms of its conical shape, highly reflective top, and internally

chaotic reflections to mud volcanoes documented elsewhere in the northern South China Sea (Sun

et al., 2012; Yan et al., 2017). It is therefore plausible SF1 could represent a mud volcano that fed

long run-out mud flows (i.e. SF2). Alternatively, the highly reflective, ribbon-like geometry of SF2

is similar to that associated with shallow/free gas accumulations (Sun et al., 2012). We consider

199 these two interpretations unlikely because: (i) the limited supply and high viscosity of mud means

200 mud volcanoes are rarely associated with long run-out flows, although we note that one mud flow

201 in the Indus Fan was ~5.0 km long (Calvès et al. 2009); and (ii) the top of SF2 is defined by a

202 positive polarity reflection (downward increase in acoustic impedance), which is opposite to that

203 typically associated with shallow/free gas accumulations (e.g. Judd and Hovland, 2007; Sun et al.,

204 2012). Based on their geometric and geophysical characteristics, spatial relationships, and similarity

205 to structures observed on other rifted continental margins, we interpret these features as volcanic

206 edifices (SF1), genetically related lava flows (SF2), and saucer-shaped shallow sills (SF3) (e.g.

207 Berndt et al., 2000; Planke et al., 2000; Thomson and Hutton, 2004; Calvès et al., 2011; Jackson,

208 2012; Magee et al., 2013; Keen et al., 2014; Reynolds et al., 2018). We now focus on the detailed

209 external morphology and internal architecture of the two deep-water volcanoes that are shallowly

210 buried (<330 m) and thus well-imaged.

211

212 **4.3. Volcano edifice 1 (V1) and associated lava flows**

213 V1 is a prominent, ~202 ms twt high (404±101 m) and ~3.0 km diameter conical volcanic edifice

214 covering ~7.2 km^2, with a volume of ~0.94±0.24 km^3 and an average flank dip of ~15.0°±3.6° (Figs.

215 3-4; Table 1). V1 is onlapped by overlying reflections, with the oldest onlapping reflection

216 correlating to TRa (~6.5 Ma); this suggests V1 was emplaced in the latest Miocene (>6.5 Ma) (Fig.

217 3a). V1 is underlain by a downward-tapering, >1.1 km deep, up to 2.0 km wide, sub-vertical zone

218 of chaotic reflections (Fig. 3a). We attribute the poor imaging within this chaotic sub-vertical zone

219 to: (1) the presence of sub-vertical feeder intrusions that disrupt background reflections and scatter

220 energy (cf. Thomson, 2007); (2) increased fluid flow and hydrothermal alteration in fractured and

221   deformed host rock adjacent to the magma plumbing system; and/or (3) scattering of energy

222   travelling through the volcano, leading to 'wash-out' of the underlying data (i.e. a geophysical

223   artefact; Magee et al. 2013). This reduction in imaging beneath the volcanoes partly obscures their

224   basal surface, but where visible it is clear BM undulates and truncates underlying stratal reflections

225   (Fig. 3b).

226   Volcano V1 is surrounded by an asymmetric apron of moderate-to-high amplitude reflections

227   extending up to 1.5 km from the main edifice. The apron is up to ~115 ms twt thick (~230±58 m),

228   and has a dip of <0.5° (Figs. 4a-b; Table 2). A package of moderate-to-very high-amplitude

229   reflections extending a further c. 1.5 km down-dip of this apron contains very high-amplitude,

230   channel-like geometries (marked C1-C3 in (Fig. 4a), which terminate down-dip into or are flanked

231   at prominent bends by, moderate-amplitude, fan-like geometries (marked F1-F4 in Fig. 4a). We

232   interpret these two features as lava flow channels and fans, respectively (Fig. 3-4). The lava flow

233   channels are sinuous, <340 m wide, and usually bisect the lava fans (Figs 4a-b). Lava flow-related

234   features (i.e. apron, channels, and fans) emanating from V1 cover an area of ~14 km^2 (Tables 3-4),

235   have an average thickness of ~33 ms twt (~66±17 m), and a volume of ~0.92±0.23 km^3; this volume

236   is nearly equal to that of V1 (~0.94±0.24 km^3) and thus represents ~50% of the total erupted volume

237   (~1.86±0.47 km^3).

238

4. 4. Volcano edifice 2 (V2) and associated lava flows

240   V2 covers ~0.44 km^2 and is elliptical in plan-view, with long and short axes of ~1.2 km and ~0.6

241   km, respectively (Figs. 5, 7). The volcano is ~100 ms twt high (~200±50 m), with an irregular base,

242   has flank dips of ~27.8°±5.9°, and a volume of 0.03±0.01 km^3 (Figs. 5, 7; Table 1). The top of V2

243 is of moderate amplitude and is irregular, with the oldest onlapping reflections correlating to

244 Reflector T1 (~5.3 Ma) suggesting V2 is latest Miocene-earliest Pliocene (>5.3 Ma), but probably

245 younger than V1 (>6.5 Ma) (Fig. 7). Reflections within V2 are chaotic and, similar to V1, V2 is

246 underlain by a vertical zone of disturbance (Fig. 7). V2 lacks a lava apron, instead being directly

247 flanked by relatively straight, >9.2 km long lava flow channels extending beyond the seismic survey

248 boundary on its south-eastern side (C4-C7) (Fig. 5a). Lava flow C6 is unusual in that underlying

249 strata are truncated at the base of the flow, defining 'ramps' that are up to~32.5 ms twt high (~65±16

250 m) and dip towards V2 at ~25.5°±5.8° (Fig. 8). Beyond the main ramp at the base of lava flow C6

251 (Fig. 5b), the lava flow thickens to ~130 ms twt (~260±65 m), where it is defined by stacked, high-

252 amplitude reflections that have a lobate geometry in plan-view (F5) (Figs. 5, 7, 8c-d). At its distal

253 end, the pinch out of F5 occurs where it abuts a basal ramp that is ~90±23 m tall and that dips

254 ~9.3°±2.3° (Figs. 8c-d). F5 is capped by a younger lava fan (F6) (Figs. 8c-d). The V2-sourced lava

255 flows (C4-C7 and F5) cover ~11.5 km^2; ~4.20 km^2 of this comprises lava flow channels and ~7.32

256 km^2 lava fan. Given the average thickness of the lava flow channels (~61±16 m) and fans (~109±27

257 m), we estimate the total volume of V2-sourced lava flows to be ~1.05±0.27 km^3; this volume

258 estimate is ~35 times greater than that of the main V2 edifice (0.03±0.01 km^3), representing ~97%

259 of the total erupted volume.

260

261 **4.5. Shallow sills and associated lava flows**

262 South of V2, we map two areally extensive, partly merged lava flows emanating from the upper

263 tips of inclined sheets fringing saucer-shaped sills (i.e. S1 and S2) (Figs. 1b, 5-6). A narrow, vertical,

264 seismically chaotic/blanking zone occurs directly below the saucer-shaped sills (Fig. 6). Several

265 linear structures, rooted at the junction between sills, and feeding the overlying lava fan (F6), are

266 also observed (Fig. 6). F6 covers an area of ~49 km^2, with a diameter of ~7.9 km and thickness of

267 55±14 m (Table 4). F6 is directly onlapped by surface T0 (~2.58 Ma), suggesting it was emplaced

268 in the latest Pliocene (>2.58 Ma) (Fig. 6). Similar to other lava fans, F6 is characterized by a single,

269 positive, high-amplitude seismic event (Fig. 6). F6 extends beyond the seismic coverage and is much

270 bigger than other lava fans imaged in the study area (Figs. 5-6; Table 4).

271

5. Discussion

5.1. Water depths during volcano emplacement

274   The different burial depths and onlap relationships of the volcano edifices and lava flows studied

275 here suggest three phases of volcanism: i.e. ~6.5 Ma for V1, ~5.3 Ma for V2, and ~2.58 Ma for

276 S1/S2 (Figs. 2-3, 6-7). According to the relative sea-level change curve of the Pearl River Mouth

277 Basin acquired from nannofossils (Xu et al., 1995; Qin, 1996) and the dating of volcanic phases, the

278 water depths during V1 and V2 emplacement were likely ~75 m and ~150 m shallower than the

279 present depths of ~2.25 km and ~2.14 km, respectively. The water depth during the emplacement of

280 F6, fed by S1/S2, was probably ~150 m greater than the present depth of ~2.32 km (Xu et al., 1995;

281 Qin, 1996). To be conservative, we estimate that volcanism in the study area occurred in water

282 depths of a little over 2.0 km.

283

5.2. Origin of post-spreading volcanism in the SCS

285   The volcanoes documented here (~6.3–2.58 Ma) have similar ages with those documented at

286 Hainan Island (e.g. Tu et al., 1991; Shi et al., 2011) and southwestern SCS (e.g. Li et al., 2013) (Fig.

1a). However, these volcanoes are substantially younger than those previously observed in the

central SCS (~13.8–7.0 Ma; Expedition 349 Scientists, 2014; Li et al., 2015) and on the middle-

lower slope of the northern SCS (~23.8-17.0 Ma; Yan et al., 2006; Zhao et al., 2016; Fan et al.,

2017). We note that the small-scale, buried, post-spreading volcanic features studied here have not

been identified by lower-resolution techniques (e.g. gravity, magnetism, OBS and 2D seismic data).

These young volcanic features may be widespread and diagnostic of post-spreading magmatism

across the northern SCS (e.g. Briais et al., 1993; Yan et al., 2006).

Given that the volcanoes documented here were emplaced after SCS rifting (>32 Ma ago; e.g.

Taylor and Hayes, 1983; Franke et al., 2014; Li et al., 2015) and spreading (>15 Ma ago; Li et al.,

2014), it is clear they have a different origin than the breakup-related volcanoes described elsewhere

(e.g. Yan et al., 2006; Expedition 349 Scientists, 2014; Li et al., 2015; Zhao et al., 2016; Fan et al.,

2017). The post-spreading age of volcanism may suggest that mantle melting (Clift et al., 2001) and

convective removal of continental lithosphere by warm asthenosphere (Lester et al., 2014),

processes typically associated with rifting and breakup, were not responsible for the generation of

this phase of igneous activity. Magmatism gets younger south-eastwards, from ~23.8–17.0 Ma on

the proximal continental slope (Yan et al., 2006; Zhao et al., 2016; Fan et al., 2017) to ~6.30–2.58

Ma in the deeper water study area. This observation is seemingly in agreement with the results of

teleseismic imaging, which shows southeastward migration of the eastern branch of the Hainan

mantle plume (Xia et al., 2016). This suggests that plume melt (Xia et al., 2016; Fan et al., 2017)

may have supplied magma to these volcanoes. However, where the Hainan mantle plume was

located or even whether the Hainan mantle plume occurred or not are still controversial at present

(e.g. Wheeler and White, 2000; He and Wen, 2011; Zhang and Li, 2018). Another possibility for

309   the origin of the magma feeding these volcanoes is related to the Dongsha Event, which may have

310   triggered mantle upwelling as well as transtensional faulting (Lüdmann et al., 1999). The Dongsha

311   Event peaked at ~5.3 Ma and 2.58 Ma (Lüdmann et al., 2001) and was broadly synchronous with

312   the main period of eruptive magmatism documented here. Faults generated during the Dongsha

313   Event may have provided high-permeability zones that promoted the vertical migration of magma

314   that fed the eruptive centers.

315

5.3. Volcano construction

317   Both V1 and V2 are underlain by sub-vertical, pipe-like zones of chaotic reflections, which we

318   suggest demarcate the limits of their magma plumbing systems. The basal surfaces of V1 and V2

319   truncate underlying strata (Figs. 3a, 7). Apparent erosion of the sub-volcanic substrate may indicate

320   the initial eruptions were explosive. Alternatively, subsidence of the volcano load into underlying,

321   wet, unconsolidated sediments may have caused the strata to locally compact and thereby change

322   the reflection configuration, making it appear that they are truncated.

323   Internal reflections that lie sub-parallel to the flanks of V1 and V2 suggest the volcanoes grew by

324   increasing both edifice height and diameter by the accretion of volcanic material (Magee et al. 2013).

325   Flank dips of ~15°–28° likely indicate that the volcanic material building the edifices constitutes

326   coherent lava flows and/or a dome structure, rather than a pyroclastic cone of tephra (Francis and

327   Thorpe, 1974; Griffiths and Fink, 1992). Construction via emplacement of coherent lava flows is

328   consistent with the presence of internal reflections in V1 and V2; i.e. boundaries between blocky

329   lava flows would be irregular and scatter seismic energy, meaning they would not likely be imaged.

330

5.4. Lava flow extrusion dynamics

In addition to the formation of volcanic edifices, both V1 and V2, as well as S1 and S2, are associated with extensive lava flows. In particular, we show V1 and V2 are flanked either by an asymmetric lava apron, which is broader on their downslope (SE) side, or lava flow channels that flowed south-eastwards for up to >9 km (Figs. 3a, 4a-b, 5a). At sub-aerial volcanoes (e.g. Walker, 1993; Cashman et al., 1999), high eruption rates and low magma viscosities are the dominant causes of long run-out lava flows. Extensive lava flows have also been observed at other deep-water volcanoes (e.g. Chadwick et al., 2018; Embley and Rubin, 2018; Ikegami et al., 2018) where greater dissolved H_2O contents in melt imply lower melt viscosity while the lavas were mobile. These low viscosity, highly mobile lavas could potentially have longer run-out distances. Higher ambient pressure can also affect bulk lava rheology, e.g. decreased vesicularity and crystal content. Lower gas fractions will also suppress magma decompression and ascent prior to eruption, and, thereby, effusion rates and extrusion dynamics (Bridges, 1997; Gregg and Fornari, 1998). For example, upon eruption of a 1200°–1100°C basalt (MORB composition) at a confining pressure of 20 MPa (i.e. a hydrostatic-equivalent water depth of 2 km), the melt can contain up to 1.4 wt% H_2O at equilibrium volatile solubility (Newman and Lowenstern, 2002). Using the viscosity model of Giordano et al. (2008) and 1.4 wt% H_2O, the resulting lava viscosity of 9–38 Pa s is significantly lower than a dry (e.g. 0.1 wt% H_2O) sub-aerial basalt, having a viscosity range of 41–248 Pa s. Higher H_2O content in lavas erupted in deep-water, compared to those extruded in sub-aerial settings, will mean: (1) there are fewer bubbles from suppressed degassing or brittle fragmentation to hinder flow (Gregg and Fornari, 1998); (2) crystallization may be inhibited, reducing the effect of crystal interactions on viscosity; and (3) the glass transition temperature is suppressed (Giordano et al. 2008), allowing

353   lavas to flow further as the interiors cool.

354   From our seismic reflection data it is also clear that channelization in lava tubes, in addition to

355   the water content effects described above, also facilitated long distance lava transport. We suggest

356   these tubes formed by rapid cooling and thickening of a surficial crust that insulated and focused

357   lava flow through a core channel (e.g. Cashman et al., 1999). Based on the long run-out lava

358   distances, we consider our initial assumption that the imaged volcanic features have a mafic

359   composition is likely. Overall, whilst we do not know the composition of the lavas imaged in our

360   seismic reflection data, pressure-related changes in lava rheology and channelization of any lava

361   type (i.e. mafic to silicic) will allow it to flow hotter for longer. Given the downslope topographic

362   control during eruption, a combination of rheology changes and channelization allowed lavas to

363   flow for >9 km from associated volcanic edifices.

364   The overall geometry and internal architecture of the imaged lava flows indicate substrate

365   rheology also controlled emplacement dynamics. Our 3D seismic reflection data show that relatively

366   long run-out lava flows (>9 km) erupted from deep-water volcanoes have a rugged basal surface

367   that is locally defined by erosional basal 'ramps'. Truncation of underlying strata suggests the lavas

368   were able to erode down into the seabed, perhaps because the pre-eruption substrate was cold, wet,

369   and unconsolidated. We suggest erosion of the lava substrate was promoted by: (1) the dense

370   (bubble-poor) lava sinking down into or 'dredging' the soft sediments (Duffield et al., 1986; Ikegami

371   et al. 2018); (2) thermal erosion (Griffiths, 2000); and/or (3) more "turbulent" flow dynamics of

372   channelized lava, consistent with the inferred low viscosities (<10 Pa s).

373   Lava flows eventually ceased in distal areas due to gradual cooling and crystallization (Cashman

374   et al., 1999). We suggest that, in the case of the straight lava flows (C5 and C6), lava transported

375   within the axial tube temporarily accumulated at the end of the flow. Lava entering the tube from

376   the ongoing volcanic eruption caused an increase in pressure, with the cooled and crystallized

377   material at the flow toe forming a transient barrier. Eventually, pressure build-up was sufficient to

378   rupture this frontal barrier, leading to emplacement of a downdip fan (F5; Fig. 5a, 7-8) (Griffiths,

379   2000). However, in the case of fans (e.g. F1-4) fed by sinuous channels (Figs. 4a-b), we suggest

380   these were emplaced in a process similar to that documented by Miles and Cartwright (2010), with

381   lobate lava flows fed and bisected by a 'lava tube' through magma inflation and increases in eruption

382   rate. At the end of sinuous lava flow channels (e.g. C1), the main channel bifurcated to form a lobate

383   fan (F3, Figs. 4a-b), which was also probably caused by flow branching triggered by magma cooling

384   (Griffiths, 2000).

385

386   **5.5. Volume balance of volcano edifice and lava flow**

387   Inaccurate constraints on total erupted volumes limits our understanding of volcano construction,

388   lava propagation, eruption rates, eruption durations, magma storage conditions, melting processes,

389   and risk assessment of volcanism in deep-water settings (Carey et al., 2018). High-resolution 3D

390   seismic reflection data allow us to calculate the volumes of material contained within volcano

391   edifices and in flanking lava flows, if they are thick enough to be imaged. In this study, we show

392   that most (i.e. 50-97%) of the erupted material was transported away from the imaged edifices. An

393   important result of our work is that flanking lava flows, and to a lesser extent the volcanic edifices,

394   have rugged and discordant bases (Fig. 7); accurately calculating the volume of deep-water

395   volcanoes and lava flows therefore requires an understanding of their pre-eruption basal morphology.

396   Erupted volume estimates based solely on remote sensing of the post-eruption seabed may be thus

397 incorrect (e.g. Robinson and Eakins, 2006). Although we show the accuracy of total erupted volume

398 estimates can be improved by constraining basal volcano and lava morphologies, seismic images

399 capturing the geological record of deep-water volcanoes cannot determine how much, if any, clastic

400 volcanic material was transported away from the eruption site as pumice rafts or through ocean

401 current clast suspension and subsequent transport (e.g. Jutzeler et al., 2014; Carey et al. 2018).

402 Nevertheless, 3D seismic imaging can significantly improve quantitative volume estimates of recent

403 and ancient volcanic edifices and lava flows, either outcropping on the seafloor or buried by

404 sedimentary successions.

405

6. Conclusions

407 High-resolution 3-D seismic data from the South China Sea allow us to image and map the

408 internal structure, calculate the volume of erupted material, and to better understand the extrusion

409 dynamics of buried deep-water volcanoes; such insights cannot readily be gained from analysis of

410 remote sensing data (e.g. airborne/shuttle radar topography). Volcanism occurred ~6.3–2.58 Ma,

411 after seafloor spreading had ceased in the area, and may be related to the Dongsha Event and/or a

412 hypothesized Hainan mantle plume. High hydrostatic pressure, an inclined seabed (~1°), and low-

413 strength, very fine-grained, near-seabed sediments, combined with formation of lava tubes and

414 extrusion of low-viscosity magmas, are likely responsible for observed long-distance lava run-outs

415 (>9 km) in this deep-water environment. We show the imaged volcanic edifices and associated lava

416 flows have rugged, erosional bases, meaning traditional remote sensing-based volume calculations

417 of deep-water volcanic features, which typically assume smooth bases, are underestimated. We

418 calculate a large amount (as high as ~97%) of the erupted materials were transported away from the

419 volcano edifices as lava flows, suggesting that volume of deep-water volcanic edifices may not

420 faithfully archive eruption size or magma production. Considering deep-water conditions (e.g. high

421 hydrostatic pressure and unconsolidated sediments) in the study area are common elsewhere, the

422 conclusions derived from this study can likely be used in other deep-water sedimentary basins and

423 perhaps sedimentary mid-ocean ridges. Our study highlights that 3D seismic reflection data can

424 contribute to understanding volcano morphology in 3D and accurately estimating the volumes of

425 erupted materials.

426

Author Contribution

428 Qiliang Sun, Christopher A-L. Jackson, Craig Magee and Xinong Xie have contributed to the

429 conceptualization, data analysis, writing and revising the original draft. Samuel J. Mitchell

430 contributed to the conceptualization and revising the original draft.

431

Competing interests

433 The authors declare that they have no conflict of interest.

434

Acknowledgment

436 This work was supported by the National Scientific Foundation of China (Grant Nos. 91528301,

437 41676051 and 41372112), the Programme of Introducing Talents of Discipline to Universities (No.

438 B14031) and the Fundamental Research Funds for the Central Universities-the China University of

439 Geosciences (Wuhan) (No. CUG160604). We thank the China National Offshore Oil Company

440 (CNOOC) for permission to release the data; reflection seismic data may be requested from CNOOC

(http://www.cnooc.com.cn/en/). Dieter Franke, Gerome Calvès and Nick Schofield are thanked for their invaluable comments and suggestions on a previous version of this manuscript. We thank Weiwei Ding, Alexander Peace, and William Chadwick for their constructive comments on this version of the manuscript, and Antonella Longo for editorial handling. Rebecca Bell is thanked for generously providing office space during the visit of Qiliang Sun to Imperial College.

References

Allen, R.W., Berry, C., Henstock, T.J., Collier, J.S., Dondin, F.J-Y., Rietbrock, A., Latchman, J.L., and Robertson, R.E.A.: 30 Years in the Life of an Active Submarine Volcano: A Time - Lapse Bathymetry Study of the Kick-'em-Jenny Volcano, Lesser Antilles, Geochem. Geophy. Geosy., 19, 715-731, https://doi.org/10.1002/2017GC007270, 2018.

Arnulf, A. F., Harding, A.J., Kent,G.M., Carbotte, S.M., Canales, J.P., and Nedimovic, M.R.: Anatomy of an active submarine volcano, Geology, 42, 655-658, https://doi.org/10.1130/G35629.1, 2014.

Berndt, C., Skogly, O.P., Planke, S., Eldholm, O., and Mjelde, R.: High-velocity break up-related sills in the Vøring Basin, off Norway, J. Geophy. Res., 105, 28443-28454, https://doi.org/10.1029/2000JB900217, 2000.

Briais, A., Patriat, P., and Tapponnier, P.: Updated interpretation of magnetic anomalies and seafloor spreading stages in the South China Sea: Implications for the Tertiary tectonics of Southeast Asia, J. Geophy. Res., 98, 6299-6328, https://doi.org/10.1029/92JB02280, 1993.

Bridges, N.T.: Ambient effects on basalt and rhyolite lavas under Venusian, subaerial, and subaqueous conditions, J. Geophy. Res., 102(E4), 9243-9255, https://doi.org/10.1029/97JE00390, 1997.

Brown, A.R.: Interpretation of three-dimensional seismic data: AAPG Memoir 42, 6thed. SEG Investigations in Geophysics, 2004.

463   Calvès, G., Schwab, A.M., Huuse, M., Clift, P.D., Gaina, C., Jolley, D., Tabrez, A.R., and Inam, A.: Seismic

464   volcanostratigraphy of the western Indian rifted margin: The pre-Deccan igneous province, J. Geophy. Res., 116,

465   B01101, https://doi.org/10.1029/2010JB000862, 2011.

466   Calvès, G., Schwab, A.M., Huuse, M., van Rensbergen, P., Clift, P.D., Tabrez, A.R., and Inam, A.: Cenozoic mud

467   volcanoe activity along the Indus Fan: offshore Pakistan, Basin Res., 22, 398-413, https://doi.org/10.1111/j.1365-

468   2117.2009.00448.x, 2009.

469   Cameselle, A.L., Ranero, C.R., Franke, D., and Barckhausen, U.: The continent-ocean transition on the northwestern

470   South China Sea, Basin Res., 29, 73-95, https://doi.org/10.1111/bre.12137, 2017.

471   Caress, D.W., Clague, D.A., Paduan, J.B., Martin, J.F., Dreyer, B.M., Chadwick Jr, W.W., Denny, A., and Kelley,

472   D.S.: Repeat bathymetric surveys at 1-metre resolution of lava flows erupted at Axial Seamount in April 2011,

473   Nat. Geosci., 5, 483-488, https://doi.org/10.1038/NGEO1496, 2012.

474   Carey, R., Soule, S.A., Manga, M., White, J.D.L., McPhie, J., Wysoczanski, R., Jutzeler, M., Tani, K., Yoerger, D.,

475   Fornari, D., Caratori-Tontini, F., Houghton, B., Mitchell, S., Ikegami, F., Conway, C., Murch, A., Fauria, K., Jones,

476   M., Cahalan, R., and McKenzie, W.: The largest deep-ocean silicic volcanic eruption of the past century, Sci. Adv.,

477   4, e1701121, https://doi.org/10.1126/sciadv.1701121, 2018.

478   Cashman, K.V., Thornber, C.R., and Kauahikaua, J.P.: Cooling and crystallization of lava in open channels, and the

479   transition of pahoehoe lava to `a`a, B. Volcanol., 61, 306-323, https://doi.org/10.1007/s004450050, 1999.

480   Chadwick Jr, W.W., Merle, S.G., Baker, E.T., Walker, S.L., Resing, J.A., Butterfield, D.A., Anderson, M.O.,

481   Baumberger, T. and Bobbitt, A.M.: A recent volcanic eruption discovered on the central Mariana back-arc

482   spreading center: Front. Earth Sci., 6, 172, https://doi.org/10.3389/feart.2018.00172, 2018.

483   Chiu, M.: The p-wave velocity modeling of the transitional crust in northern South China Sea continental margin,

484   M.S. dissertation, National Taiwan Ocean University, Keelung, 112 pp., 2010.

485 Clift, P.D., Lin, J., and ODP Leg 184 Scientific Party: Patterns of extension and magmatism along the continent-

486 ocean boundary, South China margin, Geological Society, London, Special Publications, 187, 489-510,

487 https://doi.org/10.1144/GSL.SP.2001.187.01.24, 2001.

488 Cocchi, L., Masetti, G., Muccini, F., and Carmisciano, C.: Geophysical mapping of Vercelli Seamount: Implications

489 for Miocene evolution of the Tyrrhenian back arc basin, Geosci. Front., 7, 835-849,

490 https://doi.org/10.1016/j.gsf.2015.06.006, 2016.

491 Ding, W.W., and Li, J.B.: Propagated rifting in the Southwest Sub-basin, South China Sea: Insights from analogue

492 modelling, J. Geodyn., 100, 71-86, https://doi.org/10.1016/j.jog.2016.02.004, 2016

493 Duffield, W.A., Bacon, C.R., and Delaney, P.T.: Deformation of poorly consolidated sediment during shallow

494 emplacement of a basalt sill, Coso Range, California, B. Volcanol., 48, 97-107,

495 https://doi.org/10.1007/BF01046545, 1986.

496 Embley, R.W. and Rubin, K.H.: Extensive young silicic volcanism produces large deep submarine lava flows in the

497 NE Lau Basin, B. Volcanol., 80, 36, https://doi.org/10.1007/s00445-018-1211-7, 2018.

498 Expedition 349 Scientists: South China Sea tectonics: Opening of the South China Sea and its implications for

499 southeast Asian tectonics, climates, and deep mantle processes since the late Mesozoic, International Ocean

500 Discovery Program Preliminary Report, 349, https://doi.org/10.14379/iodp.pr.349.2014, 2014.

501 Fan, C.Y., Xia, S.H., Zhao, F., Sun, J.L., Cao, J.H., Xu, H.L., and Wan, K.Y.: New insights into the magmatism in

502 the northern margin of the South China Sea: Spatial features and volume of intraplate seamounts, Geochem.

503 Geophy. Geosy., 18, 2216-2239, https://doi.org/10.1002/2016GC006792, 2017.

504 Francis, P.W. and Thorpe, R.S.: Significance of lithologic and morphologic variations of pyroclastic cones, Geo. Soc.

505 Am. Bull., 85, 927-930, https://doi.org/10.1130/0016-7606(1974)85<927:SOLAMV>2.0.CO;2, 1974.

506 Franke, D.: Rifting, lithosphere breakup and volcanism: comparison of magma-poor and volcanic rifted margins,

507   Marine and Petroleum Geology, 43, 63-87, https://doi.org/10.1016/j.marpetgeo.2012.11.003, 2013.

508   Franke, D., Savva,D., Pubellier, M., Steuer, S., Mouly, B., Auxietre, J., Meresse, F., and Chamot-Rooke, N.: The

509   final rifting evolution in the South China Sea, Mar. Petrol. Geol., v. 58, p. 704-720,

510   https://doi.org/10.1016/j.marpetgeo.2013.11.020, 2014.

511   Funck, T.: Structure of the volcanic apron north of Gran Canaria deduced from reflection seismic, bathymetric and

512   borehole data, Ph.D. dissertation, University of Kiel, 156 pp., 1996.

513   Giordano, D., Russell, J.K., Dingwell, D.B.: Viscosity of magmatic liquids: a model, Earth Planet. Sci. Lett., 271,

514   123-134, https://doi.org/10.1016/j.epsl.2008.03.038, 2008.

515   Goto, Y., and McPhie, J.: Morphology and propagation styles of Miocene submarine basanite lavas at Stanley,

516   northwestern Tasmania, Australia, J. Volcanol. Geoth. Res., 130, 307-328, https://doi.org/10.1016/S0377-

517   0273(03)00311-1, 2004.

518   Grosse, P., and Kervyn, M.: Morphometry of terrestrial shield volcanoes, Geomorphology, 304, 1-14,

519   https://doi.org/10.1016/j.geomorph.2017.12.017, 2018.

520   Greeley, R.: The role of lava tubes in Hawaiian volcanoes, U.S. Geological Survey Professional Paper 1350, 1589-

521   1602, 1987.

522   Gregg, T.K.P., and Fornari, D.J.: Long submarine lava flows: Observations and results from numerical modeling, J.

523   Geophy. Res., v. 103, p. 27517-27531, https://doi.org/10.1029/98JB02465, 1998.

524   Griffiths, R.W. and Fink, J.H.: Solidification and morphology of submarine lavas: A dependence on extrusion rate,

525   J. Geophy. Res., 97(B13), 19729-19737, https://doi.org/10.1029/92JB01594, 1992.

526   Griffiths, R.W.: The Dynamics of lava flows, Annu. Rev. Fluid Mech., 32, 477-518,

527   https://doi.org/10.1146/annurev.fluid.32.1.477, 2000.

528   Hall, R.: Cenozoic geological and plate tectonic evolution of SE Asia and the SW Pacific: Computer-based

529   reconstructions, model and animations, J. Asian Earth Sci., 20, 353-431, https://doi.org/10.1016/S1367-

530   9120(01)00069-4, 2002.

531   He, Y.M., and Wen, L.X.: Seismic velocity structures and detailed features of the D″ discontinuity near the core-

532   mantle boundary beneath eastern Eurasia, Phys. Earth Planet. In., 189, 176-184,

533   https://doi.org/10.1016/j.pepi.2011.09.002, 2011.

534   Holcomb, R.T., Moore, J.G., Lipman, P.W., and Belderson, R.H.: Voluminous submarine lava flows from Hawaiian

535   volcanoes, Geology, 16, 400-404, https://doi.org/10.1130/0091-7613(1988)016<0400:VSlava flow

536   fanH>2.3.CO;2, 1988.

537   Ikegami, F., McPhie, J., Carey, R., Mundana, R., Soule, S.A. and Jutzeler, M.: The eruption of submarine rhyolite

538   lavas and domes in the deep ocean–Havre 2012, Kermadec Arc, Front. Earth Sci., 6, 147,

539   https://doi.org/10.3389/feart.2018.00147, 2018.

540   Jackson, C.A.-L.: Seismic reflection imaging and controls on the preservation of ancient sill-fed magmatic vents, J.

541   Geol. Soc. London, 169, 503-506, https://doi.org/10.1144/0016-76492011-147, 2012.

542   Judd, A.G., and Hovland, M. (Eds.): Seabed Fluid Flow: The Impact on Geology, Biology and the Marine

543   Environment, Cambridge University Press, Cambridge, 2007.

544   Jutzeler, M., Marsh, R., Carey, R.J., White, J.D., Talling, P.J. and Karlstrom, L.: On the fate of pumice rafts formed

545   during the 2012 Havre submarine eruption. Nature communications, 5, 3660,

546   https://doi.org/10.1038/ncomms4660, 2014.

547   Keen, C.E., Dafoe, L.T., and Dickie, K.: A volcanic province near the western termination of the Charlie-Gibbs

548   Fracture Zone at the rifted margin, offshore northeast Newfoundland: Tectonics, 33, 1133-1153,

549   https://doi.org/10.1002/2014TC003547, 2014.

550   Lester, R., Van Avendonk, H.J.A., McIntosh, K., Lavier, L., Liu, C.S., Wang, T.K., and Wu, F.: Rifting and

551   magmatism in the northeastern South China Sea from wide-angle tomography and seismic reflection imaging: J.

552   Geophy. Res., 119, 2305-2323, https://doi.org/10.1002/2013JB010639, 2014.

553   Li, C.F., Lin, J., Kulhanek, D.K., and the Expedition 349 Scientists: Proceedings of the International Ocean

554   Discovery Program, 349, https://doi.org/10.14379/iodp.proc.349.103.2015, 2015.

555   Li, C.F., Xu, X., Lin, J., Sun, Z., Zhu, J., Yao, Y.J., Zhao, X.X., Liu, Q.S., Kulhanek, D.K., Wang, J., Song, T.R.,

556   Zhao, J.F., Qiu, N., Guan, Y.X., Zhou, Z.Y., Williams, T., Bao, R., Briais, A., Brown, E.A., Chen, Y.F., Clift, P.D.,

557   Colwell, F.S., Dadd, K.A., Ding, W.W., Almeida, I.H., Huang, X.L., Hyun, S., Jiang, T., Koppers, A.A.P., Li, Q.Y.,

558   Liu, C.L., Liu, Z.F., Nagai, R.H., Peleo-Alampay, A., Su, X., Tejada, M.L.G., Trin, H.S., Yeh, Y.C., Zhang, C.L.,

559   Zhang, F., and Zhang, G.L.: Ages and magnetic structures of the South China Sea constrained by the deep tow

560   magnetic surveys and IODP Expedition 349: Geochem. Geophy. Geosy., 15, 4958-4983,

561   https://doi.org/10.1002/2014JB011686, 2014.

562   Li, L., Clift, P.D., and Nguyen, H.T.: The sedimentary, magmatic and tectonic evolution of the southwestern South

563   China Sea revealed by seismic stratigraphic analysis, Mar. Geophys. Res., 34, 341-365,

564   https://doi.org/10.1007/s11001-013-9171-y, 2013.

565   Li, P., and Liang, H.: Cenozoic magmatism in the Pearl River Mouth Basin and its relationship to the basin evolution

566   and petroleum accumulation, Guangdong Geology, 9, 23-34, 1994.

567   Lüdmann, T., and Wong, H.K.: Neotectonic regime on the passive continental margin of the northern South China

568   Sea, Tectonophysics, 311, 113-138, https://doi.org/10.1016/S0040-1951(99)00155-9, 1999.

569   Lüdmann, T., Wong, H.K., and Wang, P.: Plio-Quaternary sedimentation processes and neotectonics of the northern

570   continental margin of the South China Sea, Mar. Geol., 172, 331-356, https://doi.org/10.1016/S0025-

571   3227(00)00129-8, 2001.

572   Magee, C., Hunt-Stewart, E., and Jackson, C.A.-L.: Volcano growth mechanisms and the role of sub-volcanic

573   intrusions: Insights from 2D seismic reflection data, Earth Planet. Sci. Lett., 373, 41-53,

574   https://doi.org/10.1016/j.epsl.2013.04.041, 2013.

575   Miles, A., and Cartwright, J.: Hybrid flow sills: A new mode of igneous sheet intrusion, Geology, 38, 343-346,

576   https://doi.org/10.1130/G30414.1, 2010.

577   Newman, S., and Lowenstern, J.B.: VolatileCalc: a silicate melt-H_2O-CO_2 solution model written in Visual Basic for

578   excel, Comput. Geosci., 28, 597-604, https://doi.org/10.1016/S0098-3004(01)00081-4, 2002,

579   Planke, S., Symonds, P., Alvestad, E., and Skogseid, J.: Seismic volcanostratigraphy of large-volume basaltic

580   extrusive complexes on rifted margins, J. Geophy. Res., 105, 19335-19351,

581   https://doi.org/10.1029/1999JB900005, 2000.

582   Qin, G.Q.: Application of micropaleontology to the sequence stratigraphic studies of late Cenozoic in the Pearl River

583   Mouth Basin, Marine Geology& Quaternary Geology, 16, 1-18, https://doi.org/10.16562/j.cnki.0256-

584   1492.199.04.001, 1996.

585   Reynolds, P., Holford, S., Schofield, N., and Ross, A.: Three-dimensional seismic imaging of ancient submarine lava

586   flows: an example from the southern Australian margin, Geochem. Geophy. Geosy., 18, 3840-3853,

587   https://doi.org/10.1002/2017GC007178, 2017.

588   Reynolds, P., Schofield, N., Brown, R.J. and Holford, S.P.: The architecture of submarine monogenetic volcanoes-

589   insights from 3D seismic data, Bas. Res., 30, 437-451, https://doi.org/10.1111/bre.12230, 2018.

590   Robinson, J.E., and Eakins, B.W.: Calculated volumes of individual shield volcanoes at the young end of the

591   Hawaiian Ridge, J. Volcanol. Geoth. Res., 151, 309-617, https://doi.org/10.1016/j.jvolgeores.2005.07.033, 2006.

592   Ru, K., and Pigott, J.D.: Episodic rifting and subsidence in the South China Sea, AAPG Bull., 9, 1136-1155, 1986.

593   Shi, X., Kohn, B., Spencer, S., Guo, X., Li, Y., Yang, X., Shi, H., Gleadow, A.: Cenozoic denudation history of

594   southern Hainan Island, South China Sea: constraints from low temperature thermochronology, Tectonophysics,

504, 100-115, https://doi.org/10.1016/j.tecto.2011.03.007, 2011.

Sibuet, J.-C., Yeh, Y.-C., and Lee, C.-S.: Geodynamics of the South China Sea, Tectonophysics, 692, 98-119, https://doi.org/10.1016/j.tecto.2016.02.022, 2016.

Somoza, L., Gonzalez, F.J., Barker, S.J., Madureira, P., Medialdea, T., de Ignacio, C., Lourenco, N., Leon, R., Vazquez, J.T., and Palomino, D.: Evolution of submarine eruptive activity during the 2011-2012 El Hierro event as documented by hydroacoustic images and remotely operated vehicle observations, Geochem. Geophy. Geosy., 18, 3109-3137, https://doi.org/10.1002/2016GC006733, 2017.

Sun, Q.L., Xie, X.N., Piper, D.J.W., Wu, J., and Wu, S.G.: Three dimensional seismic anatomy of multi-stage mass transport deposits in the Pearl River Mouth Basin, northern South China Sea: Their ages and kinematics, Mar. Geol., 393, 93-108, https://doi.org/10.1016/j.margeo.2017.05.005, 2017.

Sun, Q.L., Wu, S.G., Cartwright, J., Wang, S.H., Lu, Y.T., Chen, D.X., and Dong, D.D.: Neogene igneous intrusions in the northern South China Sea: evidence from high resolution three dimensional seismic data, Mar. Petrol. Geol., 54, 83-95, https://doi.org/10.1016/j.marpetgeo.2014.02.014, 2014b.

Sun, Q.L., Wu, S.G., Cartwright, J., and Dong, D.D.: Shallow gas and focused fluid flow systems in the Pearl River Mouth Basin, northern South China Sea, Mar. Geol., 315-318, 1-14, https://doi.org/10.1016/j.margeo.2012.05.003, 2012.

Sun, Z., Xu, Z., Sun, L., Pang, X., Yan, C., Li, Y., Zhao, Z., Wang, Z., Zhang, C.: The mechanism of post-rift fault activities in the Baiyun Sag, Pearl River Mouth Basin, J. Asian Earth Sci., 89, 76-87, https://doi.org/10.1016/j.jseaes.2014.02.018, 2014a.

Taylor, B., and Hayes, D.E.: Origin and history of the South China Sea Basin, in: The Tectonic and Geologic Evolution of Southeast Asian Seas and Islands, edited by Hayes, D.E.. AGU, Washington, DC, 23-56, 1983.

Thomson, K.: Determining magma flow in sills, dykes and laccoliths and their implications for sill emplacement

mechanisms, B. Volcanol., 70, 183-201, https://doi.org/10.1007/s00445-007-0131-8, 2007.

Thomson, K., and Hutton, D.: Geometry and growth of sill complexes: Insights using 3-Dseismic from the North

Rockall Trough, B. Volcanol., 66, 364–375, https://doi.org/10.1007/s00445-003-0320-z, 2004.

Tu, K., Flower, M.F.J., Carlson, R.W., Zhang, M., Xie, G.: Sr, Nd, and Pb isotopic compositions of Hainan basalts

(south China): implications for a subcontinental lithosphere Dupal source, Geology, 19, 567-569,

https://doi.org/10.1130/0091-7613(1991)019<0567:SNAPIC>2.3.CO;2, 1991.

Wang, T.K., Chen, M.K., Lee, C.S., and Xia, K.Y.: Seismic imaging of the transitional crust across the northeastern

margin of the South China Sea, Tectonophysics, 412, 237-254, https://doi.org/10.1016/j.tecto.2005.10.039, 2006.

Wang, P., Prell, W.L., and ODP 184 scientists.: Proceedings of the Ocean Drilling Program, Initial Reports, 184.

Ocean Drilling Program, College Station, TX 2000, 2000.

Walker, G.P.L.: Basaltic-volcano systems, in: Magmatic Processes and Plate Tectonics, edited by Pritchard, H.M.,

Alabaster, T., Harris, N.B.W., and Neary, C.R., Geological Society Special Publication, 76, 3-38, 1993.

Wei, X.D., Ruan, A.G., Zhao, M.H., Qiu, X.L., Li, J.B., Zhu, J.J., Wu, Z.L., and Ding, W.W.: A wide-angle OBS

profile across the Dongsha uplift and Chaoshan depression in the mid-northern South China Sea, Chinese J.

Geophys-CH., 54, 3325-3335, https://doi.org/10.3969/j.issn.0001-5733.2011.12.030, 2011.

Wu, S.G., Gao, J.W., Zhao, S.J., Lüdmann, T., Chen, D.X., and Spence, G.: Post-rift uplift and focused fluid flow in

the passive margin of Northern South China Sea, Tectonophysics, 615-616, 27-39,

https://doi.org/10.1016/j.tecto.2013.12.013, 2014.

Xia, S.H., Zhao, D.P., Sun, J.L., and Huang, H.B.: Teleseismic imaging of the mantle beneath southernmost China:

new insights into the Hainan plume, Gondwana Res., 36, 33-43, https://doi.org/10.1016/j.gr.2016.05.003, 2016.

Xie, Z.Y., Sun, L.T., Pang, X., Zheng, J.Y., and Sun, Z.: Origin of the Dongsha Event in the South China Sea: Mar.

Geophys. Res., 38, 357-371, https://doi.org/10.1007/s11001-017-9321-8, 2017.

639   Xu, S.C., Yang, S.K., and Huang, L.F.: The application of sequence stratigraphy to stratigraphic correlation, Earth

640   Sci. Front., 2, 115-123, 1995.

641   Yan, P., Deng, H., Liu, H.L., Zhang, Z., and Jiang, Y.: The temporal and spatial distribution of volcanism in the South

642   China Sea region, J. Asian Earth Sci., 27, 647-659, https://doi.org/10.1016/j.jseaes.2005.06.005, 2006.

643   Yan, P., Wang, Y.L., Liu, J., Zhong, G.J., and Liu, X.J.: Discovery of the southwest Dongsha Island mud volcanoes

644   amid the northern margin of the South China Sea, Mar. Petrol. Geol., 88, 858-870,

645   https://doi.org/10.1016/j.marpetgeo.2017.09.021, 2017.

646   Yan, P., Zhou, D., and Liu, Z.S.: A crustal structure profile across the northern continental margin of the South China

647   Sea, Tectonophysics, 338, 1-21, https://doi.org/10.1016/S0040-1951(01)00062-2, 2001.

648   Yang, S., Qiu, Y., and Zhu, B.: Atlas of Geology and Geophysics of the South China Sea, China Navigation

649   Publications, Tianjin, 2015.

650   Yu, H.S.: Structure, stratigraphy and basin subsidence of Tertiary basins along the Chinese southeastern continental

651   margin, Tectonophysics, 253, 63-76, 1994.

652   Zhang, N., and Li, Z.X.: Formation of mantle "lone plumes" in the global downwelling zone - A multiscale modelling

653   of subduction-controlled plume generation beneath the South China Sea, Tectonophysics, 723, 1-13,

654   https://doi.org/10.1016/j.tecto.2017.11.038, 2018.

655   Zhao, F., Alves, T.M., Wu, S.G., Li, W., Huuse, M., Mi, L.J., Sun, Q.L., and Ma, B.J.: Prolonged post-rift magmatism

656   on highly extended crust of divergent continental margins (Baiyun Sag, South China Sea), Earth Planet. Sci. Lett.,

657   445, 79-91, https://doi.org/10.1016/j.epsl.2016.04.001, 2016.

658   Zhao, F., Wu, S.G., Sun, Q.L., Huuse, M., Li, W., and Wang, Z.J.: Submarine volcanic mounds in the Pearl River

659   Mouth Basin, northern South China Sea, Mar. Geol., 355, 162-172, https://doi.org/10.1016./j.margeo.2014.05.018,

660   2014.

661   Zhao, S.J., Wu, S.G., Shi, H.S., Dong, D.D., Chen, D.X., and Wang, Y.: Structures and dynamic mechanism related

662   to the Dongsha Event at the northern margin of the South China Sea, Progress in Geophysics, 27, 1008-1019,

663   https://doi.org/10.6038/j.issn.1004-2903.2012.03.022, 2012.

664   Zou, H., Li, P., and Rao, C.: Geochemistry of Cenozoic volcanic rocks in Zhu Jiangkou Basin and its geodynamic

665   significance, Geochimica, 24, 33-45, 1995.

666

667

Tables

Table 1: Dimensions of volcano edifices. [a]diameter and dip are average values.

Volcano edifice	[a]Diameter (m)	Height (m)	Area (km^2)	Volume (km^3)	[a]Dip (º)
Volcano edifice 1 (V1)	3018	404±101	7.15	0.940±0.235	15.0±3.6
Volcano edifice 1 (V2)	714	200±50	0.44	0.030±0.008	27.8±5.9

Table 2: Dimensions of lava flow apron. [a]Diameter is calculated from the area as a circle. V = Volcano edifice.

Lava flow apron	Diameter (m)	Area (km^2)	Thickness (m)	Volume (km^3)	Feeder	Shape
Lava flow apron	3182[a]	7.95	80±20	0.637±0.159	V1	Ring

Table 3: Dimensions of lava flow channels (C). Please note that all the lengths of lava flow channels are measured along their axes. [a]Maximum lengths (including the inferred part of lava flow channels); [b]Minimum length (C3 extends beyond the 3D survey); [c]Thicknesses cannot be measured, because of lava flow channels (C1 and C2) are only identified on the plan-view map (RMS and variance slice map); [d]Area and volume don't include the inferred part of C5.

Lava flow channels		Length (km)	Width (m)	Thickness (m)	Area (km^2)	Volume (km^3)
Volcano edifices 1-related	C1	2.86[a]	55-273	unknown[c]	0.31[a]	unknown[c]
	C2	3.66[a]	94-340	unknown[c]	0.56[a]	unknown[c]
	C3	4.60[b]	163-340	52±13	0.84[a]	0.044±0.011
Volcano edifices 2-related	C4	2.80	172-229	61±15	0.54	0.032±0.008
	C5	9.15[a]	185-267	64±16	1.52[d]	0.097±0.024[d]
	C6	6.39	203-285	60±15	1.47	0.088±0.022
	C7	1.93	236-427	57±14	0.67	0.037±0.009

Table 4: Dimensions of lava flow fans. [a]Diameter is calculated from the area as a circle.

682 [b]Minimum areas and volumes, because of limited data coverage. C = Lava flow channel; S = Sill.

Lava flow fans	Diameter (m)	Area (km^2)	Thickness (m)	Volume (km^3)	Feeder	Shape
Lava flow fan 1 (F1)	944[a]	0.70	41±10	0.028±0.007	C1	Lobate
Lava flow fan 2 (F2)	1050[a]	0.87	41±10	0.035±0.009	C1	Lobate
Lava flow fan 3 (F3)	997[a]	0.78[b]	41±10	0.031±0.008[b]	C1	Lobate
Lava flow fan 4 (F4)	2171[a]	3.70[b]	41±10	0.148±0.037[b]	C2	Lobate
Lava flow fan 5 (F5)	3054[a]	7.32	109±27	0.791±0.198	C5/C6	Lobate
Lava flow fan 6 (F6)	7906[a]	49.07[b]	55±14	2.650±0.662[b]	S1/S2	Lobate

683

684
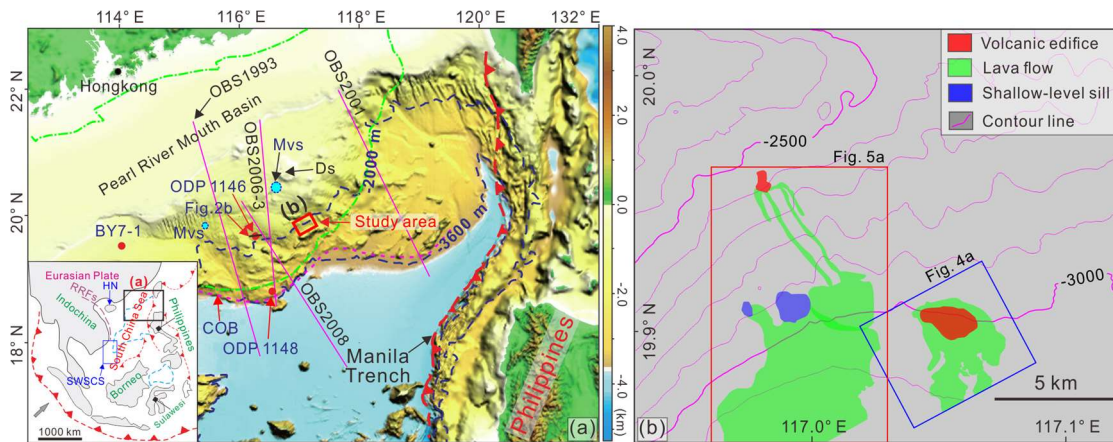
Figures

Figure 1: Geological setting of the study area. (a) Inset: regional setting of the South China Sea that

is bounded by the Red River Strike-slip faults (RRFs) to the west and by the subduction trench

(Manila Trench) to the east. Hainan Island (HN; Tu et al., 1991; Shi et al., 2011) and southwestern

South China Sea (SWSCS; Li et al., 2013) in which the magmatism has the similar ages with the

studied volcanoes are labelled in blue. In Figure (a): The study area (marked with red square) is

located to the south of Dongsha Islands (labeled Ds). The green dashed line outlines the boundary

of Pearl River Mouth Basin. Locations of boreholes (Red dots; Exploration well BY7-1 and ODP

sites 1146 and 1148), crustal structure profiles (Purple solid lines; OBS1993 (Yan et al., 2001),

OBS2001 (Wang et al., 2006), OBS2006-3 (Wei et al., 2011), and OBS2008 (Chiu, 2010)) and mud

volcanoes (Mvs) (Light blue dots; Sun et al., 2012; Yan et al., 2017) are labeled. Ds = Dongsha

Islands; COB = Continent ocean boundary (Adopted from Sibuet et al., 2016).The base map is

modified from Yang et al. (2015); (b) Seabed morphologies of the study area. Distributions of

volcano edifices (red), sills (blue), lava flows (green) and locations of Figures 4a and 5a are labeled.

The contour lines are in 100 ms (two way travel time).

703

704

705 Figure 2: (a) Synthetic seismogram of ODP Site 1146 (Modified from Sun et al., 2017); D/T =

706 Depth/time; DT =interval transit time; RHOB = lithologic density; RC = reflection coefficient; (b)

707 Seismic profile crossing through ODP Site 1146. The four seismic surfaces (T0 (~2.58 Ma), T1

708 (~5.3 Ma), TRa (~6.5 Ma) and TRb (~8.2 Ma)) are labeled; (c) Lithology and depositional

709 environment (DE) of ODP Site 1146 (Modified from Wang et al. (2000) and Clift et al. (2001)).

710

711

712

713 Figure 3: Seismic characteristics of deep-water volcano (V1) and associated lava flow channels/fans.

714 (a) Seismic profile crosscuts the volcano edifice and associated lava flow; (b) Seismic profile

715 crosscuts the lava flow (enhanced seismic anomalies). TM = top of volcano/lava flow; BM = base

716 of volcano/lava flow. See locations of seismic profiles in Figure 4.

717

718
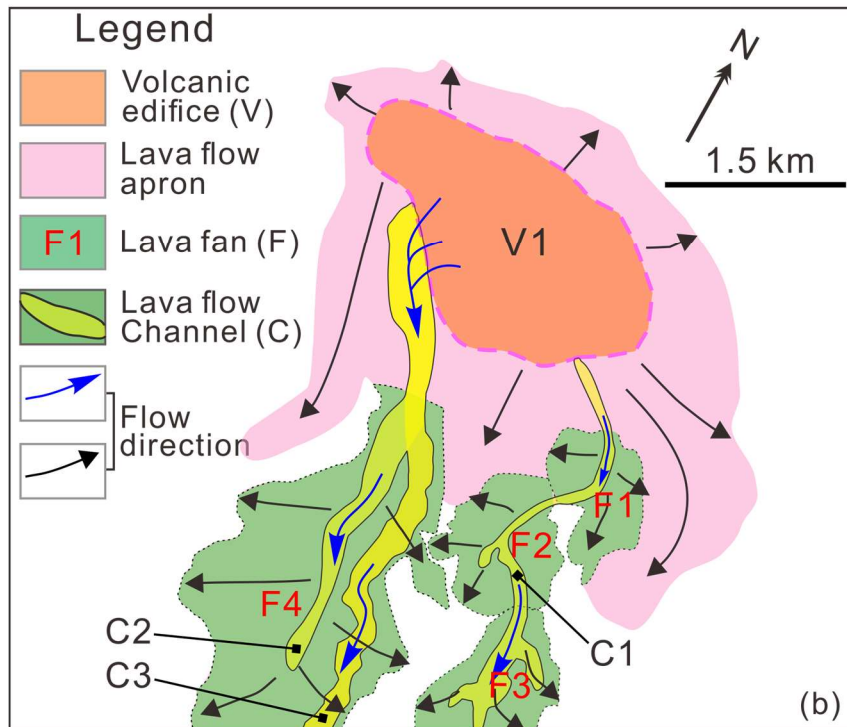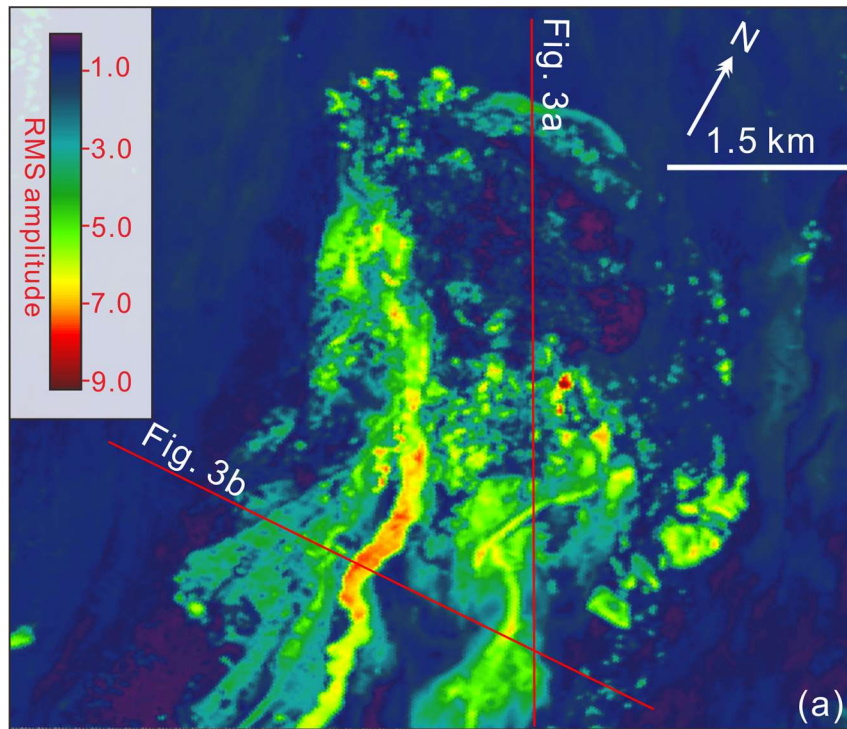
Figure 4: (a) and (b) RMS amplitude map (± 30 ms along the surface BM) and its interpretations.

Volcanic apron, lava flow channels/fans are labeled. See map location in Figure 1b. Red lines in (a)

show locations of seismic profiles in Figure 3.

723

724
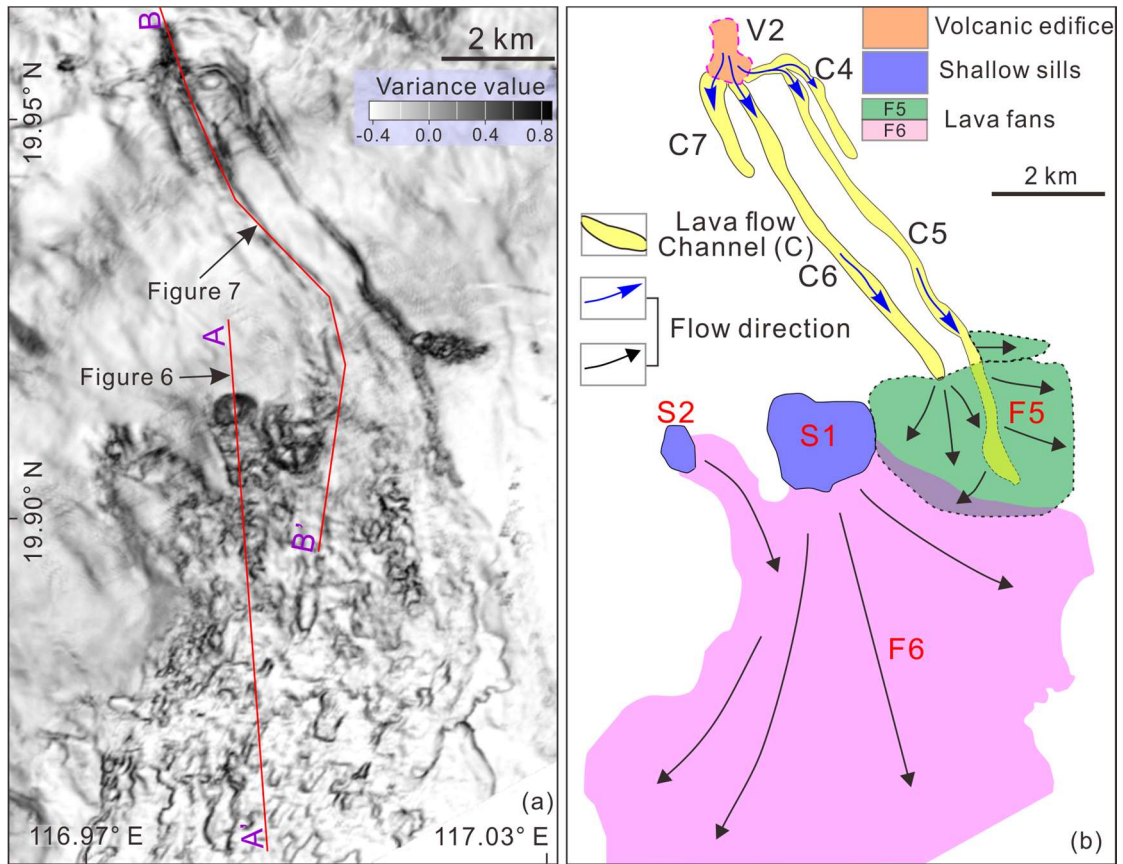
Figure 5: (a) Variance slice (extracted from the surface BM) and (b) its interpretations. Lava flows

are clearly identified by their texture and marked in (b). C = lava flow channel; S = shallow sill; F

= lava fan. Red lines A-A' and B-B' in (a) are seismic profiles shown in Figures 6 and 7.

728

729

730
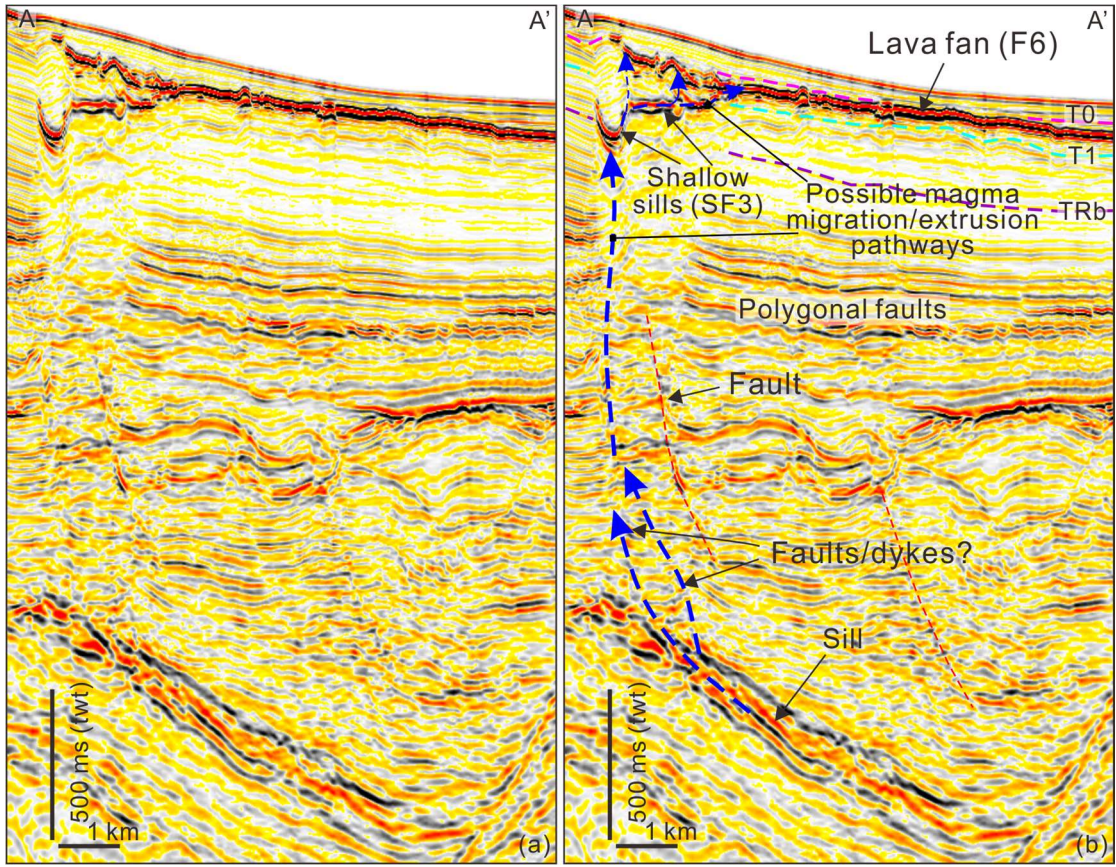
Figure 6: (a) Seismic profile and (b) its interpretation show magma pluming system from deep-

732   seated sill, shallow sill (S1) and lava fan (F6). See location of seismic profile A-A' in Figure 5a.

733

734

735
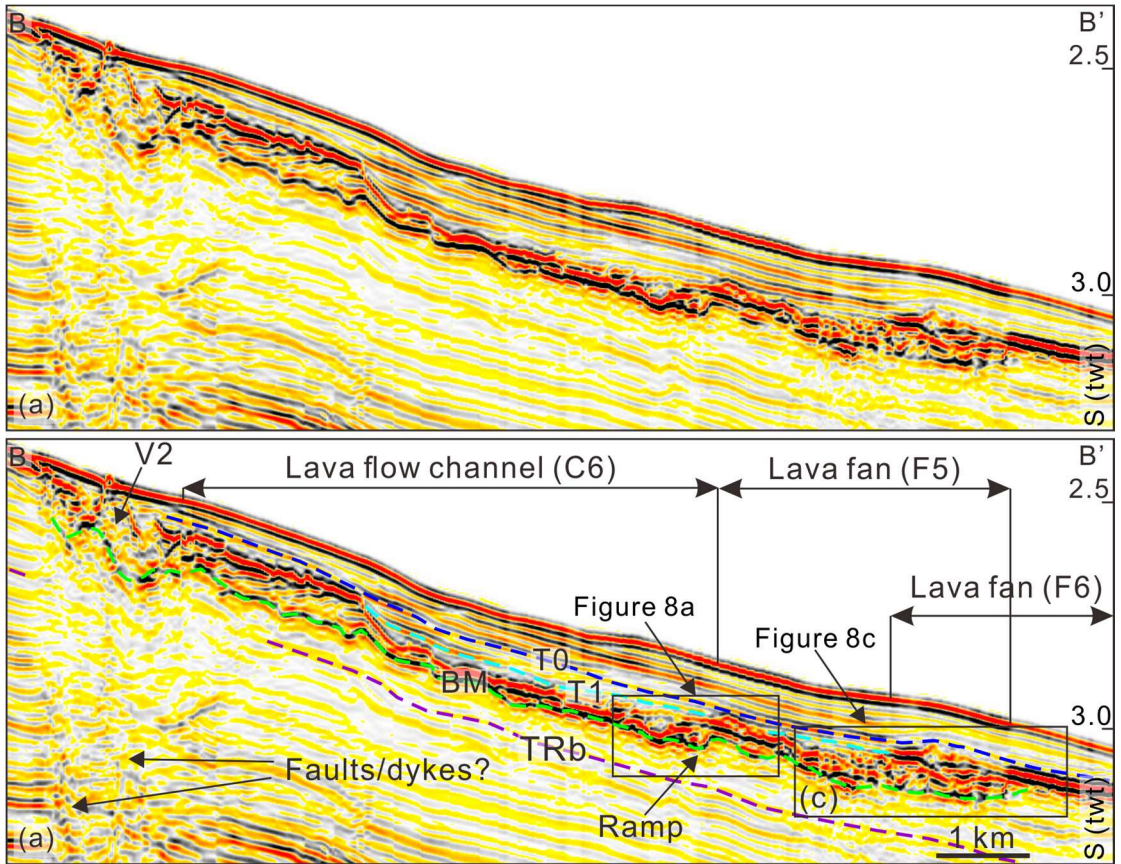
Figure 7: (a) Seismic profile crosscuts V2 and along lava flow channel (C6) and Lava fans (F5 and

F6). The V2 has a sharp boundary to the upslope. Lava fan 6 (F6) is directly overlying the Lava fan

5 (F5). BM = base of volcano/lava flow; See location of seismic profile B-B' in Figure 5a.

739
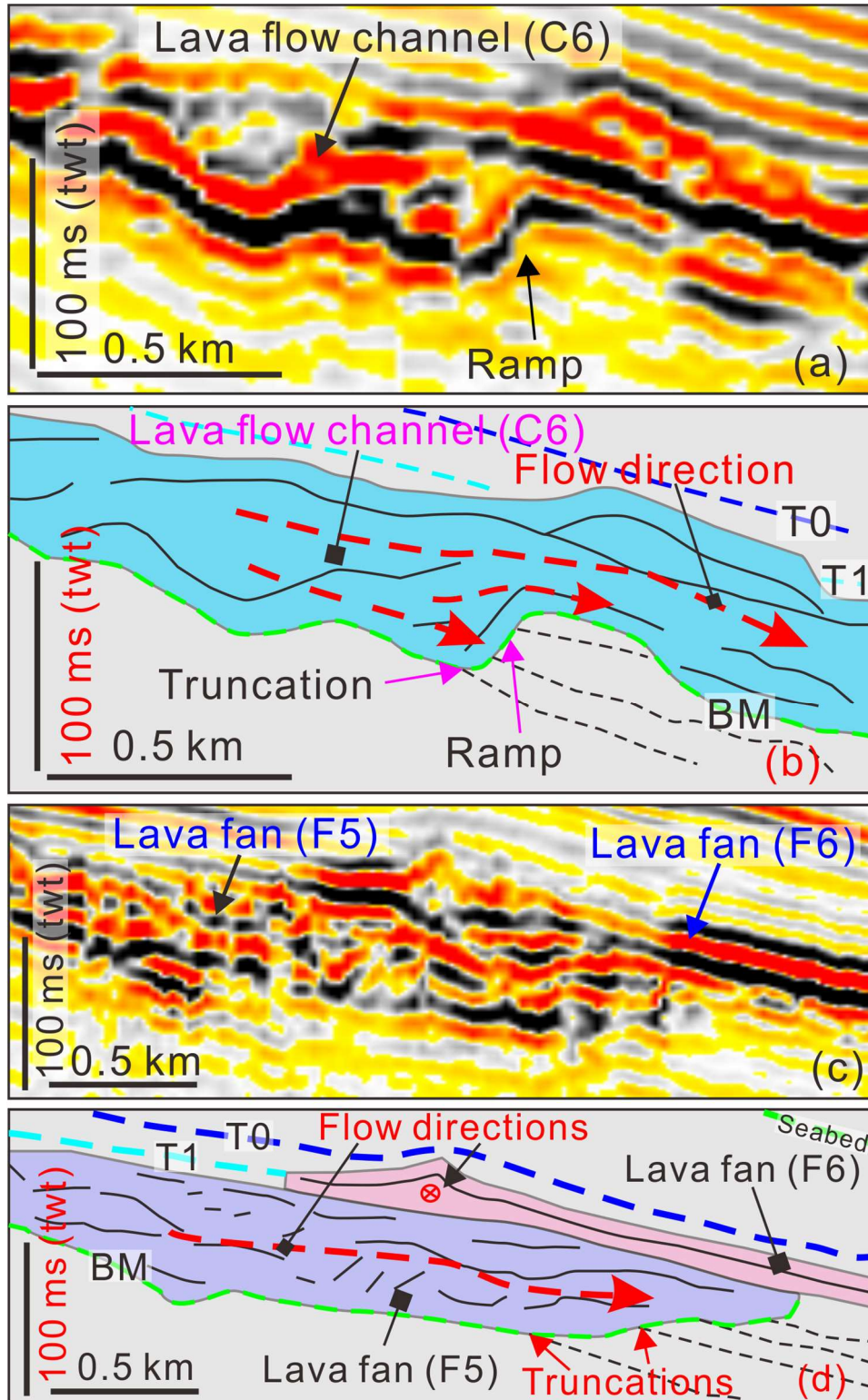
Figure 8: (a) and (b) Enlargement of the end of lava flow channel (ramp structure) and its line drawings; (c) and (d) Enlargement and its line drawings of the lava fans (F5 and F6). BM = base of volcano/lava flow. See locations in Figure 7.